# The GASS/EUCLIPSE Model Intercomparison of the Stratocumulus Transition as Observed During ASTEX: LES results

J. J. van der Dussen,[1] S. R. de Roode,[1] A. S. Ackerman,[2]

P. N. Blossey,[3] C. S. Bretherton,[3] M. J. Kurowski,[4,5] A. P. Lock,[6]

R. A. J. Neggers,[7] I. Sandu[8] and A. P. Siebesma[7,1]

Corresponding author: J. J. van der Dussen, Department of Geoscience and Remote Sensing, Delft University of Technology, Stevinweg 1, Delft, 2628 CN, The Netherlands. (j.j.vanderdussen@tudelft.nl)

[1]Delft University of Technology, Delft,

**Abstract.** Large eddy simulation (LES) results of a transition from a relatively well-mixed to a thin, decoupled stratocumulus layer with cumulus cloud penetration from below, are compared to aircraft observations collected during the Atlantic Stratocumulus Transition Experiment (ASTEX). Despite the complexity of the case and the long simulation period of 40 hours, the six participating state-of-the-art models skilfully represent the observed evolution of the boundary layer, including the gradual deepening of the bound-

The Netherlands

[2]National Aeronautics and Space Administration (NASA) Goddard Institute for Space Studies (GISS), New York, USA

[3]University of Washington, Seattle, USA

[4]University of Warsaw, Warsaw, Poland

[5]Institute of Meteorology and Water Management–National Research Institute, Warsaw, Poland

[6]Met Office, Exeter, UK

[7]Royal Netherlands Meteorological Institute (KNMI), De Bilt, The Netherlands

[8]Max-Planck Institut für Meteorologie (MPI-H), Hamburg, Germany

ary layer, the negative buoyancy flux at the top of the subcloud layer and the development of the double peaked vertical velocity variance profile. The turbulent moisture transport to the stratocumulus layer shows a clear diurnal cycle, indicating that during daytime moisture builds up in the subcloud layer. However, during the night the moisture flux at cloud base exceeds the surface evaporation, causing the liquid water path (LWP) to increase. Even though the models agree on the bulk features of the transition, the spread in the LWP and the entrainment rate during the first 12 hours is large. It is argued that this spread is mainly attributable to differences in the parametrized precipitation rate. Because thicker clouds absorb more solar radiation and hence evaporate more, the LWP spread diminishes rapidly during the day. The simulation results therefore suggest that the details of the microphysics parametrization are of little importance to the timing of the stratocumulus cloud breakup.

## 1. Introduction

Large portions of the Earth's oceans are covered by fields of stratocumulus clouds [*Wood*, 2012]. As these clouds are advected towards the equator by the trade winds, they are gradually replaced by trade cumuli, that have a much lower area coverage. The radiative signature of both clouds types, therefore, is very different, which makes the accurate representation of the transition between them important for the performance of numerical weather and global climate models. *Teixeira et al.* [2011] show that the negative bias in the low cloud amount many such models have, is partly attributable to the transition from stratocumulus to trade cumulus in the subtropics, which occurs too early as compared to observations.

Several studies have been devoted to the modelling of these cloud transitions. Most of these studies utilized 1D or 2D turbulence models [e.g. *Krueger et al.*, 1995; *Bretherton and Wyant*, 1997; *Wyant et al.*, 1997; *Bretherton et al.*, 1999; *Svensson et al.*, 2000], as the available computational resources at the time, were insufficient to perform 3D simulations on a sufficiently large domain for the typical timespan of a cloud transition, which is of the order of days.

Owing to the continuous advance in the amount of available computational power, such 3D simulation have now become feasible in the form of Large Eddy Simulation (LES), as is demonstrated by *Sandu and Stevens* [2011]. The results show that LES models are well capable of representing the smooth transition between the two cloud regimes. However, as a drawback of the composite approach on which basis the simulation cases were set up [*Sandu et al.*, 2010], it is not possible to compare the simulation results to detailed in-situ measurements.

Recently, *Chung et al.* [2012] performed idealize LES simulations of the stratocumulus transition in an idealized Eulerian framework, by prescribing a range of sea surface temperatures and running until a statistical steady state, similar to the setup used by *Zhang et al.* [2010]. The cloud types found in the steady state solutions range from a relatively well-mixed stratocumulus, via cumulus under stratocumulus to a cumulus topped boundary layer, thereby corroborating the finding of *Sandu and Stevens* [2011], that sea surface temperature increase is the main cause of the stratocumulus transition. This is in agreement with research by *Medeiros and Stevens* [2011], who show that the most important factor separating cumulus and stratocumulus regimes is the lower tropospheric stability.

Aircraft observations of a stratocumulus transition were performed during the first Lagrangian experiment of the Atlantic Stratocumulus Transition EXperiment (ASTEX) measurement campaign [*Albrecht et al.*, 1995; *Bretherton and Pincus*, 1995; *Bretherton et al.*, 1995; *De Roode and Duynkerke*, 1997]. During this Lagrangian, a transition was observed from a solid stratocumulus topped boundary layer to a boundary layer dominated by cumulus clouds below a thin veil of broken stratocumulus.

Within the Global Energy and Water Cycle Experiment (GEWEX) Cloud System Study working group (GCSS), a model intercomparison study for 1- and 2-dimensional turbulence models was set up by *Bretherton et al.* [1999] based on this first Lagrangian measurement series. It was shown that all models were able to predict the deepening and decoupling of the boundary layer and the cumuli appearing below the stratocumulus clouds. Significant quantitative differences in liquid water path and cloud cover were ascribed to the parametrisations of radiation, microphysics and subgrid scale turbulence.

Additionally, two intercomparison studies for LES models were organised on the basis of the second (A209) and the third flight [RF06, *Duynkerke et al.*, 1999] of the first Lagrangian. The results show that the entrainment in the models was on average about 50 % larger than the entrainment rate estimated from the measurements. Including cloud microphysics, and, to a lesser extent, increasing the vertical resolution, was shown to decrease the entrainment velocity.

Based on the experience gained from these previous ASTEX intercomparison projects, in this paper, a revised model set-up for LES and Single Column Models (SCMs) is described, based on the 40 h period between measurement flights 2 and 5. The entire transition as observed during the first Lagrangian experiment of ASTEX is run using LES models for the first time. The six participating state-of-the-art LES models now include detailed parametrisation schemes for radiation and microphysics, and high resolutions are used to better resolve the entrainment process at the boundary layer top. Geostrophic winds are furthermore prescribed, such that no relaxation towards observations is required, in contrast to the original set-up described by *Bretherton et al.* [1999].

Together with the three composite cases designed by *Sandu and Stevens* [2011], this case is run as a joint GEWEX Atmospheric System Study (GASS) and European Union CLoud Intercomparison, Process Study and Evaluation (EUCLIPSE) project effort, to evaluate how well stratocumulus transitions are represented by LES as well as Single Column Model (SCM) versions of operational weather forecasting and climate models.

The results will be reported in three parts. This paper contains the set-up of the ASTEX case, as well as a detailed comparison of the results with the available observations, in order to give an impression of how well the models are able to represent the measurements. A second paper contains the LES results of all four cases and will concentrate on the general behaviour of the models during stratocumulus transitions in terms of bulk features [*Sandu and Stevens*, 2011; *De Roode et al.*, 2012], which will provide a basis for the evaluation of the SCM results in the third paper.

The following section contains information on the simulation set-up: the initial profiles and the boundary conditions as well as numerical aspects such as resolution and domain size. In Section 3, the shows the results submitted by the participating modellers as well as the observations. The last section contains a summary of the main conclusions and some discussion.

## 2. Setup

### 2.1. Initial conditions

The simulations start 13 June 1992 at 0000 UTC (2300 h local time) and last 40 h, approximately corresponding to the time between ASTEX measurement flights 2–5. The first flight, which took place during the afternoon and evening of June 12th is disregarded, as, during this period, the boundary layer structure was inhomogeneous, with occasionally small cumuli and fog [*De Roode and Duynkerke*, 1997]. During the second flight, the stratocumulus-topped boundary layer was more well-mixed and horizontally homogeneous, making this flight more suitable as a starting point than the first.

Initial profiles are taken from an earlier GCSS intercomparison case, which was set-up by Peter Duynkerke:

$$\varphi(z) = \begin{cases} \varphi_{\mathrm{ml}} & z \le z_i \\ \varphi_{\mathrm{ml}} + \Delta\varphi(z - z_i)/\Delta z & z_i < z \le z_i + \Delta z \\ \varphi_{\mathrm{ml}} + \Delta\varphi + \\ \quad \Gamma_\varphi(z - z_i - \Delta z) & z_i + \Delta z < z \le 2\,\mathrm{km} \end{cases} \tag{1}$$

where $\varphi \in \{q_T, \theta_L, u, v\}$, respectively the total specific humidity, the liquid water potential temperature and the velocities in east-west and south-north directions. Initial values of the mixed layer variables $\varphi_{\mathrm{ml}}$, the inversion jumps $\Delta\varphi$ and the vertical gradient $\Gamma_\varphi$ for each of these variables are given in Table 1. Initially, the inversion layer has a thickness of $\Delta z = 50\,\mathrm{m}$ and its base is at a height $z_i = 662.5\,\mathrm{m}$. The initial profile for the pressure is constructed by assuming hydrostatic equilibrium, with a surface pressure $p_s = 1029.0\,\mathrm{hPa}$, which is constant in time.

Plots of the profiles defined by Eq. (1) are shown in Figure 1 together with the observations from which the profiles were originally derived. Above 2 km, the profiles are determined from ERA-Interim reanalysis data, as described in Section 2.2.4. The initial profiles, as well as the forcings described below, can be downloaded from the EUCLIPSE project website[1].

### 2.2. Model forcings

During ASTEX, observations were performed in a Lagrangian way, which means that a column of air was followed as it was advected towards the equator. An advantage of this approach is that the effect of horizontal advection on the budgets of heat and moisture can be neglected, provided the vertical shear of horizontal winds is negligibly small. To account for changing conditions along the Lagrangian trajectory, time-varying forcings and boundary conditions are prescribed. Using these forcings, no relaxation towards the observations is required, in contrast to the earlier ASTEX model intercomparison case described by *Bretherton et al.* [1999].

#### 2.2.1. Sea surface temperature

For the simulations, the sea surface temperature compiled by *Bretherton et al.* [1995, Figure 1a] is used, which contains reanalysis data supplied by the ECMWF and measurements from both aircraft and a ship. This data gives a relatively fast increase of about 4 K over the 40 hour simulation period. Note that, for the GCSS LES intercomparison cases based on flights A209 and RF06, surface fluxes were prescribed instead of the surface temperature.

#### 2.2.2. Geostrophic wind

During the transition, the horizontal velocities in the boundary layer and in the free atmosphere changed in direction from mainly north to north-east as can be seen in Figure 2a. The magnitude of the total velocity relative to the surface changed from approximately $10\,\mathrm{m\,s^{-1}}$ to $4\,\mathrm{m\,s^{-1}}$. For the calculation of the surface fluxes of heat and moisture, it is important to include this change, which is done by prescribing time-dependent geostrophic winds. The required geostrophic winds can be estimated from the observed free atmospheric velocities using:

$$\frac{\partial u_{\mathrm{fa}}}{\partial t} = \quad f(v_{\mathrm{fa}} - v_g) \tag{2a}$$

$$\frac{\partial v_{\mathrm{fa}}}{\partial t} = -f(u_{\mathrm{fa}} - u_g), \tag{2b}$$

in which the subscript 'fa' indicates free atmospheric values, $f$ is the Coriolis parameter and $u_g$ and $v_g$ are the horizontal components of the geostrophic wind.

Time series of the prescribed geostrophic winds, which are constant with height, can be found in Figure 2, together with the observed wind velocities during the research flights, averaged over the boundary layer and over the free atmosphere separately. Also shown in the plot are the expected wind velocities in the free atmosphere, found from integration of Eqs. (2).

From Figure 2 it is furthermore clear that in the observations, the wind shear over the inversion is generally less than $2\,\mathrm{m\,s^{-1}}$, suggesting that the influence of horizontal advection of $q_T$ and $\theta_L$ is small.

Surface fluxes are calculated using a surface roughness length $z_0 = 2 \times 10^{-4}\,\mathrm{m}$, independent of the wind speed.

### 2.2.3. Large scale divergence

For the GCSS model intercomparison cases based on flights A209 and RF06, the divergence was chosen such that the modelled entrainment rate approximately balanced the mean vertical wind velocity, in order to keep the inversion height constant during the 3 hour long simulations. However, the negligence of cloud droplet sedimentation and precipitation processes as well as the coarse vertical grid spacing caused the models to over-entrain. It is therefore likely that the prescribed divergence rates of $5 \times 10^{-6}\,\mathrm{s}^{-1}$ and $15 \times 10^{-6}\,\mathrm{s}^{-1}$ for the A209 and RF06 cases respectively, are too high.

Later, *Bretherton et al.* [1999] derived the divergence shown in Figure 2a from measurements and ECMWF reanalysis data. *De Roode and Van der Dussen* [2010] showed that, using this divergence, the boundary layer grows unrealistically fast in the second half of the simulation, resulting in a boundary layer that is almost 1 km deeper than the one observed.

*Ciesielski et al.* [1999] used soundings of the horizontal velocities to calculate the average vertical velocity and divergence for the period 1-15 June 1992. Their results show only a slight and gradual decrease in divergence during the first Lagrangian, resulting in an average value of about $4 \times 10^{-6}\,\mathrm{s}^{-1}$. This is in line with the conclusion of *Sigg and Svensson* [2004], who state that there is no evidence for the strong decrease in divergence that was suggested by *Bretherton and Pincus* [1995].

Figure 2b shows the divergence diagnosed from ERA-Interim data. The spatial and temporal variations in the data are large, as is the case with ERA-40 data [*Duynkerke et al.*, 1999], causing the boundary layer averaged divergence at the column's position to fluctuate between about $5 \times 10^{-6}$ and $-1 \times 10^{-6}\,\mathrm{s}^{-1}$. *Ciesielski et al.* [2001] find a diurnal signal in the divergence, with an amplitude of up to $2 \times 10^{-6}\,\mathrm{s}^{-1}$ and a similar diurnal cycle has been proposed in other studies [e.g. *Bretherton et al.*, 2004], but due to the low temporal resolution, something similar cannot be discerned in the ERA-Interim data. When the divergence is averaged over the ASTEX triangle, the signal fluctuates less and seems to decrease slightly during the period of the First Lagrangian.

Finally, based on these data, a divergence rate is prescribed that decrease linearly with time from a value of $5 \times 10^{-6}\,\mathrm{s}^{-1}$ to $1 \times 10^{-6}\,\mathrm{s}^{-1}$ and following *Bretherton et al.* [1999], the divergence is put to zero from 1600 m up, which produces realistic $q_T$ and $\theta_L$ tendencies in the free atmosphere.

### 2.2.4. Radiation

Radiative transfer codes are used to provide accurate temperature tendencies due to longwave and shortwave radiation in the LES domain. The background profiles of humidity, temperature and ozone, required by these schemes have been determined from ERA-Interim reanalysis data and are constant in time. The influence of the low amount of cirrus clouds that was observed at the end of the Lagrangian [*Ciesielski et al.*, 1999], is neglected for simplicity.

An important factor for the calculation of both radiative and microphysical effects on the cloud layer is the size of the cloud droplets. The cloud droplet number density $N_c$ is assumed to be constant at $100\,\mathrm{cm}^{-3}$ [*Bretherton et al.*, 1995] wherever liquid water is present. A log-normal cloud droplet size distribution is assumed, resulting in a correction factor for the calculation of the effective radius $r_e$ that is a function of geometric standard deviation $\sigma_g$. Using $\sigma_g = 1.2$:

$$r_e = r_V \exp\left[\ln(\sigma_g)^2\right] \approx 1.03\, r_V. \quad (3)$$

in which $r_V$ is the mean volume radius of the droplets:

$$r_V = \left(\frac{3\rho_a q_L}{4\pi\rho_L N_c}\right)^{1/3}, \quad (4)$$

where $\rho_a$ and $\rho_L$ are the densities of respectively moist air and liquid water and $q_L$ is the liquid water specific humidity. The value of 1.03 in Eq. 3 is in good agreement with observational findings by *Pawlowska and Brenguier* [2000].

The sea surface albedo $\alpha_s$ is a function of $\mu$, the cosine of the solar zenith angle, and is approximated by [*Briegleb*, 1992]:

$$\alpha_s = \frac{0.026}{\mu^{1.7} + 0.065} + 0.15(\mu - 0.10)(\mu - 0.50)(\mu - 1.00). \tag{5}$$

### 2.3. Numerical and model details

Results from six different LES models were submitted. References to the descriptions of these models can be found in Table 2, together with any remarks regarding differences between the code used and the existing documentation.

The domain used here is identical to that used by *Sandu and Stevens* [2011] and consists of 128×128 grid boxes with a resolution $\Delta x$, $\Delta y = 35\,\mathrm{m}$ resulting in a horizontal domain size of $4480^2\ \mathrm{m}^2$. In the $z$-direction a resolution is used varying from 15 m at the surface to 5 m in the cloud layer and at the inversion. Above 2400 m, at the base of the sponge layer, the grid is stretched by increasing $\Delta z$ by 10 % per level.

It is recognised that the horizontal size of the domain is rather limited. The high vertical resolution necessary to properly resolve the large gradients in the inversion layer, however, limits the maximum time-step of integration to less than 1 s. The combination with the 40 h duration makes these simulations computationally demanding. *Sandu and Stevens* [2011] performed simulations on a larger domain of $8.96^2\ \mathrm{km}^2$ and found that cases with little precipitation hardly differed from the small domain simulations.

The domain is translated with a constant velocity of $-2\,\mathrm{m\,s^{-1}}$ in the $x$- and $-7\,\mathrm{m\,s^{-1}}$ in the $y$-direction. These velocities are chosen as optimal values for computational efficiency.

All modellers where asked to provide the same output data as in the RICO (Rain in Cumulus over the Ocean) model intercomparison [*vanZanten et al.*, 2011].

## 3. Model results and observations

### 3.1. Observations

In this section, the LES results are compared with observations gathered during the ASTEX Lagrangian measurement series on which this case is based. The simulations span the period between the second (A209) and the fifth flight (A210) of this experiment. A summary of the flights, the periods during which they took place and the part of the simulation approximately corresponding to the flights is given in Table 3. In Sections 3.3 and 3.4 the observations are compared to model results averaged over the periods mentioned in this table.

The measurements of the mean state variables (Section 3.3), performed during the horizontal, the profiling and the porpoising legs of the respective flights, have been bin-averaged over height intervals of 100 m and a standard deviation of each of these bins was calculated. The turbulence state variables (Section 3.4) were derived from time series measurements taken during horizontal flight legs, each with a length of about 60 km. Fluctuations with respect to a running average with a length of 3 km were calculated by *De Roode and Duynkerke* [1997]. They estimated the sampling error in the second order moments to be about 20 % for flights RF06 and RF07, and between 10 and 40 % for flight A210. Due to technical limitations, the humidity fluxes are unreliable in-cloud, in particular for the RF flights and are therefore disregarded [*Wang and Lenschow*, 1995]. More reliable measurements have been made using a CSIRO sensor, but due to the low measurement frequency of 1 Hz, much of the small scale transport is not measured, likely causing a strong low bias.

### 3.2. Timeseries

Figure 3 shows snapshots of the 3D liquid water specific humidity field, which includes rain water, at hours 8, 19 and 36 of the transition, as simulated using the Dutch Atmospheric LES (DALES). These snapshots give a good overview of the transition: the gradually deepening boundary layer, the thinning stratocumulus layer and the development of cumulus updraughts penetrating the cloud layer. Finally cloud free areas appear, indicating the onset of the breaking up of the cloud layer.

In Figure 4, the cloud cover (top) and the cloud contours (bottom) are shown for each of the participating models. The contours of the cloud layer are composed of the inversion height $z_i$ (upper set of lines), to indicate the average stratocumulus cloud top, minimum cloud base height $z_{b,\mathrm{min}}$ (lowest set) and the domain averaged cloud base height $z_b$ (middle set).

As the simulation progresses, the mean cloud base height keeps increasing, whereas the minimum cloud base height is approximately constant. The large separation between these heights in the second half of the simulation is indicative of the decoupling of the boundary layer and the development of saturated updrafts below the stratocumulus layer. The general picture of the transition is consistent in the models. Differences in minimum (cumulus) cloud base height are negligible, while the spread in the modelled inversion height and average cloud base height is of the order of 200 m, which is about 20 % of the total inversion height increase over the course of the transition.

A plot of the entrainment rate $w_e$ as a function of time is shown in Figure 5a, including estimates made on the basis of observations [*De Roode and Duynkerke*, 1997]. The diurnal cycle is clearly visible in this plot, with significantly more entrainment during the night compared to the daytime.

It will be argued in Section 4.4 that microphysical processes are the major cause of the significant model spread in the entrainment rate that is present during the initial 10 hours. The inclusion of precipitation is also an important cause of the decreased entrainment rate as compared to the GCSS model intercomparison study based on flight RF06 (hour 8), in which microphysical processes were not taken into account. *Duynkerke et al.* [1999] reported an average entrainment rate of about $1.9\,\mathrm{cm\,s^{-1}}$ for this case, which was recognised to be high compared to the observed value of about $1.2\,\mathrm{cm\,s^{-1}}$. The average entrainment rate presented here is, at about $1.4\,\mathrm{cm\,s^{-1}}$, much better in line with the observations. Other contributors to the decrease of the entrainment rate are: the inclusion of cloud base warming, which was previously neglected, and a higher vertical resolution of $5\,\mathrm{m}$ compared to the $25\,\mathrm{m}$ resolution used by *Duynkerke et al.* [1999]. The combination of this lower entrainment rate and the revised large scale divergence rate results in a boundary layer deepening rate that is in good agreement with the observations.

Figure 5b shows the liquid water path LWP, which is defined as:

$$\mathrm{LWP} = \int_0^\infty \rho_a q_L \mathrm{d}z. \tag{6}$$

Note that $q_L$ also includes rain water. Estimates derived from the measured average liquid water specific humidity profiles are indicated by squares.

During the night, the models show a steady or increasing LWP, despite the boundary layer decoupling evident in Figure 4. As the sun rises, approximately 8 h after the start of the simulation, the LWP starts to decrease, to a local minimum approximately 2-3 hours after local noon. At this point, the large spread in the model results of over $100\,\mathrm{g\,m^{-2}}$ during the first night has also decreased significantly.

The decrease of the model spread can be explained by the fact that thicker clouds tend to absorb more solar radiation. This effect is illustrated by the plot in Figure 6, which shows the difference in the total shortwave radiative flux between the top and the base of an idealized stratocumulus layer as a function of the LWP, assuming a cloud droplet number density $N_c = 100\,\mathrm{cm}^{-3}$ and without considering rain water. The amount of absorbed solar radiation increases with LWP over the entire range. Models with a high LWP during the first night, such as DHARMA and UCLA LES, therefore have a much sharper drop in LWP as the sun rises than for instance DALES. As the largest differences in LWP occur during the night, the consequences for the cloud albedo are low. The maximum albedo difference between the models is less than 0.10. During the simulated part of the transition, the top of the atmosphere albedo decreases from an diurnally averaged 0.45 to approximately 0.15 to 0.20 in all models.

Figure 6 also shows the difference in the total longwave radiative flux between the stratocumulus top and base. For LWP $> 25\,\mathrm{g\,m}^{-2}$, this difference is almost independent of LWP. This due to the fact the cloud layer emits radiation approximately as a black body, independent of the depth of the layer.

For LWP $\lesssim 20\,\mathrm{g\,m}^{-2}$ (corresponding to a cloud layer thickness of approximately 140 m), the cloud layer becomes optically thin, reducing the emission at cloud top (as well as the absorption at cloud base) of longwave radiation. Longwave cooling maintains the stratocumulus cloud layer by driving the vertical mixing that provides the moisture from below, as well as by cooling the cloud layer. The loss of these mechanisms, in combination with continued entrainment warming and drying, causes the stratocumulus layer to rapidly dissolve and breakup.

This effect is visible in the simulation results from DHARMA, for which the LWP drops below $20\,\mathrm{g\,m^{-2}}$ around hour 30, after which the cloud cover quickly reduces to about 5 to 10 %.

### 3.3. Mean state vertical profiles

Figure 7 shows domain averaged profiles of thermodynamic state variables $q_T$, $\theta_L$, $q_L$ and the horizontal velocities $u$ and $v$ averaged over the hours corresponding to ASTEX research flights RF06, RF07 and A210 (Table 3). Bin-averaged measurements are indicated by squares and the $\pm$ one standard deviation range of each bin is shown using error bars.

In the free atmosphere, the combination of the prescribed subsidence rate and the radiative cooling rates calculated by the models, results in an appropriate evolution of the free atmospheric temperature and humidity. Furthermore, the change of the horizontal velocities $u$ and $v$ in time are close to those observed. Unfortunately, no measurements have been taken above the boundary layer height of about 1800 m during flight A210 (hour 36). The simulated temperature and humidity profiles in the boundary layer during the first half of the simulation agree well with the observations, with maximum humidity and temperature differences staying well within $1\,\mathrm{g\,kg^{-1}}$ and 1 K, respectively. This result is surprising, considering the complexity of the case, the diversity of parametrisation schemes used in the models and the relatively long simulation time compared to preceding LES intercomparison cases.

The most noticeable difference between model results and observations during hours 8 and 19 is the strength of the gradients of $q_T$ and $\theta_L$ in the inversion layer. Most probably, this discrepancy is the result of the higher degree of horizontal inhomogeneity in the observed air mass, possibly on a large scale. Due to the limited simulation domain, such inhomogeneities cannot be represented by the models. The result is that the simulated liquid water specific humidity profiles in Figures 7c and 7g have sharper peaks, located more toward the top of the boundary layer as compared to the average observed profiles. During the last flight, the temperature and humidity differences between models and observations are significantly larger than during the first half of the transition. It should be noted in this respect, that many of the legs flown during flight A210 were cloud free, and significantly warmer and less moist than the cloudy legs. Temperature excursions of the order of 1 K were measured over distances of more than 50 km. This mesoscale variability complicates the comparison of the models with the observations. The warming at the top of the boundary layer for the results of DHARMA after the break-up of the stratocumulus layer, indicates that cloud free areas in the models also tend to be relatively warm. Another possible explanation for the temperature difference between the model results and the observations is that the appearance of cirrus clouds, which were observed during the last flight, caused the downwelling longwave radiative flux to increase. Consequently, the divergence of longwave radiation over the cloud layer decreases, which leads to less cooling and therefore to a relatively warm boundary layer.

The evolution of the boundary layer profiles shows great similarity with the conceptual model of the vertical structure of decoupled boundary layers, as proposed by *Wood and Bretherton* [2004, Figure 1]. Starting from a relatively shallow, well-mixed boundary layer, slowly a three-layered structure develops as the boundary layer deepens. The sub-cloud at the bottom of the boundary layer and the stratocumulus layer at the top, both are relatively well-mixed and connected by a cumulus layer. The bulk of the turbulent transport through this layer is governed by few cumulus updraughts. Without exception, the models reproduce this change of the boundary layer structure very well.

### 3.4. Turbulence state vertical profiles

The turbulence state of the atmosphere during the flights is summarised by the profiles shown in Figure 8.

The gradual decrease in time of the horizontally averaged turbulent kinetic energy $e$, found in the observations, is reproduced by the models, as can be seen in Figures 8a, 8d and 8h. As the transition progresses, the $e$ profiles in both the models and the observations develop a minimum in the middle of the boundary layer, indicative of a lower degree of turbulent mixing at the interface between the cloud and the subcloud layer.

The profiles of the vertical velocity variance $\sigma_w^2$, which constitutes an important part of turbulent kinetic energy, show this decreased turbulent mixing in the decoupled layer more clearly. The single peaked Figure 8b indicates that during the first night, the boundary layer remains relatively well-mixed. The observations however seem to indicate a more well-mixed structure, which could be caused by the lower boundary layer height. Models that generate much precipitation, for instance DALES and SAM, also tend to have a lower vertical velocity variance and a more decoupled structure.

After the first day (Figure 8f), between approximately 400 and 700 m height, a decoupled layer has developed in which the turbulence intensity on average is low. The subcloud layer below and the stratocumulus layer above this layer remain well-mixed, resulting in the typical double peaked profile. This profile is in very good agreement with the observations, especially in the subcloud layer.

The skewness of the vertical velocity $S_w$, here defined as:

$$S_w = \frac{\overline{w'^3}}{\sigma_w^3}, \tag{7}$$

increases steadily during the simulations. In the first part of the transition (Figure 8d), the negative skewness caused by downdraughts originating from the inversion almost completely cancels against the positive effect of updraughts from the surface, resulting in a small skewness in the middle of the boundary layer. In the models, updraughts seem to be more dominant than the observations indicate.

At the end of the transition, cumulus clouds with strongly buoyant cores start occurring. The high vertical velocities of these cores constitute the tail of the probability distribution of $w$, causing the skewness to peak in the middle of the boundary layer (see Figure 8l). A distinct minimum in the skewness profile can be found at the top of the subcloud layer. The profiles of $\overline{w'\theta_V'}$ (Figures 8c, 8g and 8k) show that these negative buoyancy fluxes at cloud base are present throughout the transition, but are strongest at the onset of decoupling. It has been suggested that this turbulence decoupling leads to a drying of the cloud layer and causes the rapid break up of the cloud [see e.g. *Nicholls*, 1984; *Bretherton and Wyant*, 1997]. The results for this transition, however, indicate that even when the boundary layer is decoupled, stratocumulus clouds can persist for a day or more.

In the layer between the subcloud and the stratocumulus cloud layer, buoyancy fluxes are found to be slightly positive (see Figures 8g and 8k), due to a low area fraction of strongly buoyant updraughts.

As the boundary layer gets more decoupled, the subcloud layer exhibits clear convective boundary layer behaviour, with an approximately parabolic $\sigma_w^2$ and a linear buoyancy flux profile, with slightly negative values at the top of the mixed layer. This feature seems to be very robust as the spread in the model results is small, and the agreement with the observations is striking.

Another feature that is well represented by the models is the peak in the buoyancy flux profile at hour 19. All models show a similar peak with approximately the same magnitude, although there is some spread in the height at which it is located, which is caused by the spread in the inversion height among the models.

The buoyancy peak is located at the top of the stratocumulus cloud layer, where the virtual potential temperature flux can be written in terms of fluxes of $\theta_L$ and $q_T$, as follows

$$\overline{w'\theta'_V}_{\mathrm{top}} = A_w \overline{w'\theta'_L}_{\mathrm{top}} + B_w \overline{w'q'_T}_{\mathrm{top}}. \tag{8}$$

Here, $A_w \approx 0.5$ and $B_w \approx 1000\,\mathrm{K}$ are thermodynamic coefficients for a saturated environment. Assuming a quasi-steady state, the fluxes of $q_T$ and $\theta_L$ in the stratocumulus cloud layer, close to the inversion can be approximated as follows:

$$\overline{w'q'_T}_{\mathrm{top}} = -w_e \Delta q_T + \Delta F_p; \tag{9}$$

$$\overline{w'\theta'_L}_{\mathrm{top}} = -w_e \Delta\theta_L + \frac{1}{\rho c_p}\Delta F_r - \frac{L_v}{c_p}\Delta F_p. \tag{10}$$

In this equation, $\Delta$ denotes the difference between a variable just above and just below the inversion layer. Furthermore, $F_r$ is the total radiative flux in $\mathrm{W\,m^{-2}}$ and $F_p$ is the precipitation flux (negative downwards). The subscripted 'top' denotes variables at the top of the boundary layer.

By substituting Eqs. (9) and (10) into Eq. (8), the following can be written:

$$\begin{aligned}\overline{w'\theta'_V}_{\mathrm{top}} = & - w_e \left(A_w \Delta\theta_L + B_w \Delta q_T\right) + \frac{A_w}{\rho c_p}\Delta F_r \\ & + \left(B_w - A_w \frac{L_v}{c_p}\right)\Delta F_p.\end{aligned} \tag{11}$$

As $A_w L_v / c_p \approx 1250\,\mathrm{K} > B_w$, precipitation always reduces the buoyancy flux in the cloud layer $\overline{w'\theta'_V}_{\mathrm{top}}$.

According to Eq. (11), the increase of the buoyancy flux between hours 8 and 19 can be attributed to, in the first place, the strengthening of the inversion jump of $q_T$ from approximately $-2$ to $-3\,\mathrm{g\,kg^{-1}}$, which is apparent from Figure 7. A second cause for the increase of $\overline{w'\theta'_V}_{\mathrm{top}}$ is the decrease of the precipitation rate between the mentioned hours.

## 4. Humidity Budget

### 4.1. Budget closure

Following the approach of *Bretherton et al.* [1995] the different terms of the humidity budget from the LES models can be compared to the observations.

From Figure 4 and 7, it can be seen that the modelled total humidity in the boundary layer as well as the deepening rate of the boundary layer are in good agreement with the observations. Other processes determining the humidity budget of the boundary layer are the surface humidity flux and the precipitation rate.

In the following sections, the model results for these processes are discussed and compared to the observations. Sensitivity experiments are performed in order to investigate the range of uncertainty resulting from the case setup.

### 4.2. Surface latent heat flux

Figure 9 shows time-series of the modelled surface sensible (shf) as well as the surface latent heat flux (lhf). Measured values, derived from the flight legs performed closest to the surface (mostly around 30 m) are indicated by circles (shf) and squares (lhf). During the initial 10 hours of the simulation, the surface lhf increases to approximately 100 W m$^{-2}$ due to the increase of both the sea surface temperature and the horizontal wind speed, according to the well-known bulk formula for the turbulent flux of humidity at the surface:

$$\overline{w'q_T'}|_0 = C_q|\mathbf{u}|_{\mathrm{sl}}\left\{q_{\mathrm{sat}}(T_s) - q_{T,\mathrm{sl}}\right\}, \tag{12}$$

in which $C_q$ is the bulk transfer coefficient for moisture, $|\mathbf{u}|$ is the magnitude of the horizontal wind vector, $q_{\mathrm{sat}}(T_s)$ is the saturation specific humidity for the temperature of the surface ($T_s$). The subscripted 'sl' denotes the surface layer.

During the second part of the transition, the total wind speed decreases considerably (see

Figure 2a), causing the lhf to decrease to around $50\,\mathrm{W\,m^{-2}}$.

It is obvious from Figure 9 that the surface lhf in the models is much larger than in the observations. This result is surprising, considering the fact that the modelled humidity and horizontal velocities close to the surface agree well with the observations, judging from Figure 7. Furthermore, using the Clausius-Clapeyron equation, the reported uncertainty of about $0.5\,\mathrm{K}$ in the surface temperature [*Bretherton et al.*, 1995], can be shown to cause an uncertainty of approximately $0.45\,\mathrm{g\,kg^{-1}}$ in $q_{\mathrm{sat}}$. This translates to an uncertainty of $15\,\%$ in the modelled surface flux, if no other variables are influenced.

The remaining parameter in Eq. (12) is the bulk transfer coefficient for moisture $C_q$. This transfer coefficient is determined among others from the surface roughness length $z_0$, which was prescribed to be constant at $0.2\,\mathrm{mm}$, a value typically used for open sea conditions. In reality however, $z_0$ is mainly determined by the wave height, which is a function of the horizontal wind velocity close to the surface. This effect is described by the Charnock relation:

$$z_0 = \frac{\alpha_c u_*^2}{g}, \tag{13}$$

in which $u_*$ is the friction velocity, $g$ is gravitational acceleration, and $\alpha_c$ is the Charnock parameter, the value of which varies among models: $0.011 \lesssim \alpha_c \lesssim 0.018$ [*Renfrew et al.*, 2002]. Using a typical value $\alpha_c = 0.015$ results in $z_0 \approx 0.17\,\mathrm{mm}$ during the first 20 hours of the simulation, which is slightly lower than the prescribed constant value. The low wind speeds encountered towards the end of the transition, decrease $z_0$ to about $0.03\,\mathrm{mm}$. Tests performed using DALES indicate that using the Charnock relation instead of the constant $z_0$ effect neither the LWP nor the moment of stratocumulus cloud breakup significantly. However, it does results in a decrease of the surface lhf by up to $15\,\%$.

Apart from Charnock's relation, SCMs often use a lower value of the surface roughness length for moisture and heat than for momentum [see also *Vickers and Mahrt*, 2010, for observational evidence]. Therefore, an additional test was performed in which $z_{0q,h} = z_{0m}/10$ was used. Again, a reduction of the lhf of about 10 -15 % was found. As a result of this reduction, the subcloud layer becomes considerably dryer by about $0.5\,\mathrm{g\,kg^{-1}}$, which is in better agreement with the observations than the results of the reference simulation, as can be seen in Figure 11.

### 4.3. Moisture flux at stratocumulus cloud base

As can be seen from the profiles in Figure 10, the observed lhf is not only lower than in the models at the surface, but throughout the entire subcloud layer. As was mentioned above, the observations derived from (partly) cloudy aircraft legs are unreliable and therefore disregarded following *Wang and Lenschow* [1995].

In the stratocumulus layer, where the cloud fraction is approximately one, $\overline{w'q'_T}$ can also be estimated from observed $\overline{w'\theta'_V}$ and $\overline{w'\theta'_L}$ fluxes using Eq. (8), resulting in maximum values of around $100\,\mathrm{W\,m^{-2}}$ in the stratocumulus layer at hour 19, which are more in line with measurements in the subcloud layer as well as with the model results.

The modelled flux profiles in Figure 10 do not show the strongly decoupled structure as suggested by *Nicholls* [1984] or *Bougeault* [1985], with humidity fluxes going to zero at the top of the subcloud layer. The domain averaged fluxes have hardly visible minima in the middle of the boundary layer, indicating that much of the moisture evaporating from the surface is transported to the cloud layer, despite the turbulence decoupling that is obvious in the buoyancy flux profiles.

In order to quantify how much of the moisture reaches the stratocumulus layer, $r_{q_T}$ is defined as the ratio of the moisture flux at the mean cloud base $z_b$ over the flux at the surface:

$$r_{q_T} = \frac{\overline{w'q'_T}(z_b)}{\overline{w'q'_T}(0)}. \tag{14}$$

This ratio is plotted in Figure 12. A clear diurnal cycle is visible in this figure, with high values exceeding unity during the night and a distinct minimum during the first day. This suggests that the effect of decoupling is strong at daytime, when the moisture flux at cloud base is about 50 % of that at the surface, but much more limited during the nights. For the initial 24 hours of the transition $r_{q_T} \approx 0.95$, averaged over all models.

### 4.4. Precipitation

The surface precipitation flux as a function of time is shown in Figure 13b. During the first night, this flux is relatively large, with domain averaged values of up to $30\,\mathrm{W\,m^{-2}}$ ($\approx 1\,\mathrm{mm\,d^{-1}}$). During the first day, however, as the cloud layer thins, hardly any drizzle reaches the surface any more.

Especially at hours 8 and 19, the observed precipitation rates are much higher than in the models. The quality of those measurements however is questionable, as there are large differences between the precipitation rates at mean cloud base and at the surface, as can be seen in Figure 13.

Simple precipitation parametrisations have been developed on the basis of several measurement campaigns [see *Geoffroy et al.*, 2008, for a review]. Here the relation between the precipitation rate, the LWP and the cloud droplet number density $N_c$ derived by *Comstock et al.* [2004] is used, which can be written as:

$$\rho L_v F_p(z_b) = 10.8 \left(\frac{\mathrm{LWP}}{N_c}\right)^{1.75}, \tag{15}$$

where $(\rho L_v F_p)$, LWP and $N_c$ are in $\mathrm{W\,m^{-2}}$, $\mathrm{g\,m^{-2}}$ and $\mathrm{cm^{-3}}$ respectively. For this transition, a similar relation by *vanZanten et al.* [2005] gives almost identical results.

Figure 13a shows the precipitation rate at cloud base calculated using Eq. (15) (black dots) for the observed values of the LWP and $N_c = 100\,\mathrm{cm^{-3}}$, together with model results and direct observations (squares). The error bars span the range of observed droplet number densities $N_c$=50-150 $\mathrm{cm^{-3}}$ (upper and lower bounds, respectively) as reported by *Bretherton and Pincus* [1995]. The results calculated using the parametrisation of Eq. (15) show a trend that is consistent with the LES results and hint at an overestimation of the direct ASTEX observations.

Among the model results, initially there are significant differences in the precipitation rates. Models that are less prone to produce rain, allow the LWP to grow during the first night (compare Figure 5). As the LWP increases, these models also start producing rain. Eventually (around hour 10), most models have similar precipitation rates, but at different values of the LWP.

The consequences of the spread in the precipitation rate in the models for the LWP are clear from the scatter plot in Figure 14. This figure shows the LWP as a function of the precipitation rate at stratocumulus cloud base, both averaged over the first 12 hours of the transition. Additional simulations were performed with DALES, using three different values of $N_c$, namely 60, 100 (reference) and 200 $\mathrm{cm^{-3}}$. In addition to the scheme by *Khairoutdinov and Kogan* [2000, KK00, hereafter], which was used for the reference simulation, the simulations were also performed using the scheme of *Seifert and Beheng* [2001, SB01]. The top axis of the Figure 14 shows the LWP tendency due to precipitation:

$$\left[\frac{\mathrm{d\,LWP}}{\mathrm{d}t}\right]_{\mathrm{driz}} = -\frac{F_p(z_b)}{L_v} \qquad (16)$$

in units of $\mathrm{g\,m^{-2}\,h^{-1}}$ [*Van der Dussen et al.*, 2012]. Based on these tendency numbers, the expected LWP difference between for instance the UCLA LES and DALES results over the 12 hour period is approximately $250\,\mathrm{g\,m^{-2}}$.

A secondary effect, however, of a higher precipitation rate is a decrease of the entrainment rate, as was already shown by *Nicholls* [1984] and *Chen and Cotton* [1987], among others. *Ackerman et al.* [2004] therefore argue that the LWP response to increased precipitation is the result of the competition between the increased removal of liquid water from the boundary layer and the reduced drying due to the lower entrainment rate. For ASTEX, the free atmosphere is relatively moist, such that the former response is dominant.

Figure 15 shows that the average entrainment rate indeed decreases with increased precipitation rate. Considering the multitude of processes through which microphysics impact on the boundary layer dynamics [*Ackerman et al.*, 2009], it is striking to see that the models results exhibit this strong correlation between precipitation rate at cloud base and entrainment rate. The scatter plots in Figure 14 and 15 furthermore suggest that the significant spread among the model results in the LWP and entrainment rate during the first 12 hours, is attributable to the differences among the microphysics parametrization schemes.

The simulation results nevertheless indicate that the pace of the transition is hardly related to the microphysical details of the models, since SAM, MOLEM, UCLA LES and DALES all breakup at approximately the same time (see Figure 4), despite their strongly varying precipitation rates. This is basically due to the strong decrease of the LWP during the first day. The remaining veil of stratocumulus cloud at the top of the boundary layer after this first day is too thin to support significant amounts of precipitation, such that the differences among the models vanish.

## 5. Discussion and Conclusions

In this study, the stratocumulus transition as observed during the ASTEX field experiment is simulated using six LES models. The model results agree unexpectedly well, especially considering the complexity of the case, including multiple time-varying boundary conditions, a diurnally varying radiative forcing, the included parametrisation of microphysical processes and the long simulation time of 40 hours. Four of the models agree to within one hour on the moment of stratocumulus cloud breakup and the spread in the inversion height among the models is generally of the order of 200 m over a total increase of over 1000 m.

The results of the models are furthermore compared to the measurements taken during three aircraft flights, that were performed at different moments during the transition. All participating models were able to closely reproduce the rate of boundary layer deepening as well as the mean state vertical structure of the observed boundary layer throughout the simulation. Observed features of the boundary layer turbulence, such as the strong increase of the buoyancy flux at the top of the boundary layer and the development of a double peaked vertical velocity variance profile, are also present in the models.

As there are indications that the chosen value for the surface roughness length for moisture is too high, a sensitivity test was performed using DALES. This simulation shows that reducing this roughness length by a factor of 10 gives a reduction of surface latent heat flux by about 15 %, without significantly affecting the moment of cloud breakup. More importantly, the subcloud humidity at the end of the transition is decreased by about $0.5\,\mathrm{g\,kg^{-1}}$, which diminishes the apparent moist bias of the models compared to the observations.

By defining a ratio of the turbulent humidity flux at cloud base over that at the surface, the turbulence decoupling of the boundary layer is shown to exhibit a clear diurnal cycle. During the day, the transport of humidity from the surface to the cloud layer is limited, such that the subcloud layer moistens. During the night, the turbulent moisture flux at stratocumulus cloud base is shown to exceed that at the surface, which indicates that cumuli resupply the stratocumulus cloud layer with moisture from the subcloud layer [*Martin et al.*, 1995; *Chung et al.*, 2012].

The largest source of spread among the models was argued to be in the parametrisation of microphysical processes. The substantial differences in LWP (exceeding $100\,\mathrm{g\,m^{-2}}$) and entrainment rate (about $0.3\,\mathrm{cm\,s^{-1}}$) among the models during the first night are shown to be strongly related to the precipitation flux at stratocumulus cloud base. Additional sensitivity simulations using DALES indicate that a simple changing from the *Khairoutdinov and Kogan* [2000] to the *Seifert and Beheng* [2001] microphysics scheme results in a reduction of the precipitation flux of about 50 %. Unfortunately, the quality of the precipitation measurements is questionable, as the observed fluxes are much higher than would be expected on the basis of research by *Comstock et al.* [2004] among others. As there is no clear reference for the precipitation rate, no microphysics scheme can be preferred above another on the basis of this intercomparison study.

As the sun rises during the first day, the intermodel differences in the LWP are diminished, as models with a high LWP tend to absorb more radiation and therefore lose more $q_L$. During the subsequent night, the low LWP suppresses much of the precipitation formation, such that the spread among the models remains relatively small.

A remaining question for this ASTEX case is the cause of the large temperature differences between the models and the observations at the end of the transition. The simulated boundary layer at that time is several degrees cooler than the observations, which might be due to the appearance of cirrus clouds or due to mesoscale organisation, which cannot be represented on the limited horizontal domain size used for this study.

The results of this research show that much progress has been made in the modelling of stratocumulus transitions since the previous intercomparison cases based on ASTEX [*Duynkerke et al.*, 1999; *Bretherton et al.*, 1999]. This progress is mainly attributable to the availability of sufficient computational power to perform these multi-day simulations using a full 3D LES model instead of 1D or 2D models, at high resolution. Other important improvements are the incorporation of advanced parametrisation schemes for radiation and precipitation as well as the use of prescribed sea surface temperatures, as compared to the prescribed surface flux forcing used in the previous LES intercomparison studies based on A209 and RF06. While there is still room for improvement in, in particular, the parametrisation of precipitation and the model resolution [*Yamaguchi and Randall*, 2012], the current results give enough confidence to use LES model results as a benchmark for the evaluation of the performance of SCMs in stratocumulus transitions.

**Acknowledgments.** The research leading to these results has received funding from the European Union, Seventh Framework Programme (FP7/2007-2013) under grant agreement n° 244067. ECMWF ERA-Interim data used in this project have been obtained from the ECMWF data server. The work was sponsered by the National Computing Facilities Foundation (NCF) for the use of supercomputer facilities. We kindly thank Coen Hennipman and Arjan van Leeuwen for providing analysis used in this paper and Gunilla Svensson for helpful suggestions regarding the setup of the case.

## Notes

1. `www.euclipse.nl/wp3/ASTEX_Lagrangian/LES_astex_setup.shtml`

## References

Abel, S. J., and B. J. Shipway (2007), A comparison of cloud-resolving model simulations of trade wind cumulus with aircraft observations taken during RICO, *Quart. J. Roy. Meteor. Soc.*, *133*(624), 781–794.

Ackerman, A. S., M. P. Kirkpatrick, D. E. Stevens, and O. B. Toon (2004), The impact of humidity above stratiform clouds on indirect aerosol climate forcing, *Nature*, *432*(7020), 1014–1017.

Ackerman, A. S., M. C. vanZanten, B. Stevens, V. Savic-Jovcic, C. S. Bretherton, A. Chlond, J.-C. Golaz, H. Jiang, M. Khairoutdinov, S. K. Krueger, D. C. Lewellen, A. Lock, C.-H. Moeng, K. Nakamura, M. D. Petters, J. R. Snider, S. Weinbrecht, and M. Zulauf (2009), Large-eddy simulations of a drizzling, stratocumulus-topped marine boundary layer, *Mon. Wea. Rev.*, *137*(3), 1083–1110.

Albrecht, B. A., C. S. Bretherton, D. Johnson, W. H. Scubert, and A. S. Frisch (1995), The Atlantic stratocumulus transition experiment–ASTEX, *Bull. Amer. Meteor. Soc.*, *76*(6), 889–904.

Blossey, P. N., and D. R. Durran (2008), Selective monotonicity preservation in scalar advection, *J. Comput. Phys.*, *227*(10), 5160–5183.

Bougeault, P. (1985), The diurnal cycle of the marine stratocumulus layer: A higher-order model study, *J. Atmos. Sci.*, *42*(24), 2826–2843.

Bretherton, C. S., and R. Pincus (1995), Cloudiness and marine boundary layer dynamics in the ASTEX lagrangian experiments. part I: Synoptic setting and vertical structure, *J. Atmos. Sci.*, *52*(16), 2707–2723.

Bretherton, C. S., and M. C. Wyant (1997), Moisture transport, lower-tropospheric stability, and decoupling of cloud-topped boundary layers, *J. Atmos. Sci.*, *54*(1), 148–167.

Bretherton, C. S., P. Austin, and S. T. Siems (1995), Cloudiness and marine boundary layer dynamics in the ASTEX lagrangian experiments. part II: Cloudiness, drizzle, surface fluxes, and entrainment, *J. Atmos. Sci.*, *52*(16), 2724–2735.

Bretherton, C. S., S. K. Krueger, M. C. Wyant, P. Bechtold, E. Van Meijgaard, B. Stevens, and J. Teixeira (1999), A GCSS boundary-layer cloud model intercomparison study of the first ASTEX Lagrangian experiment, *Bound.-Layer Meteor.*, *93*(3), 341–380.

Bretherton, C. S., T. Uttal, C. W. Fairall, S. E. Yuter, R. A. Weller, D. Baumgardner, K. Comstock, R. Wood, and G. B. Raga (2004), The epic 2001 stratocumulus study, *Bull. Amer. Meteor. Soc.*, *85*(7), 967–977.

Briegleb, B. P. (1992), Delta-eddington approximation for solar radiation in the ncar community climate model, *J. Geophys. Res.*, *97*(D7), 7603–7612.

Chen, C., and W. R. Cotton (1987), The physics of the marine stratocumulus-capped mixed layer, *J. Atmos. Sci.*, *44*(20), 2951–2977.

Chung, D., G. Matheou, and J. Teixeira (2012), Steady-state large-eddy simulations to study the stratocumulus to shallow cumulus cloud transition, *J. Atmos. Sci.*, *69*(11), 3264–3276.

Ciesielski, P. E., W. H. Schubert, and R. H. Johnson (1999), Large-scale heat and moisture budgets over the ASTEX region, *J. Atmos. Sci.*, *56*(18), 3241–3261.

Ciesielski, P. E., W. H. Schubert, and R. H. Johnson (2001), Diurnal variability of the marine boundary layer during ASTEX, *J. Atmos. Sci.*, *58*(16), 2355–2376.

Comstock, K. K., R. Wood, S. E. Yuter, and C. S. Bretherton (2004), Reflectivity and rain rate in and below drizzling stratocumulus, *Quart. J. Roy. Meteor. Soc.*, *130*(603), 2891–2918.

De Roode, S. R., and P. G. Duynkerke (1997), Observed lagrangian transition of stratocumulus into cumulus during ASTEX: Mean state and turbulence structure, *J. Atmos. Sci.*, *54*(17), 2157–2173.

De Roode, S. R., and J. J. Van der Dussen (2010), Large-eddy simulation of a stratocumulus to cumulus cloud transition as observed during ASTEX, in *Proceedings of the 19th Symp. Bound.-Layers and Turbulence*, Keystone.

De Roode, S. R., I. Sandu, J. J. van der Dussen, A. S. Ackerman, P. N. Blossey, A. Lock, A. P. Siebesma, and B. Stevens (2012), LES results of the EUCLIPSE Lagrangian stratocumulus to shallow cumulus transition cases, in *20th Symposium on Boundary Layers and Turbulence*.

Duynkerke, P. G., P. J. Jonker, A. Chlond, M. C. Van Zanten, J. Cuxart, P. Clark, E. Sanchez, G. Martin, G. Lenderink, and J. Teixeira (1999), Intercomparison of three- and one-dimensional model simulations and aircraft observations of stratocumulus, *Bound.-Layer Meteor.*, *92*(3), 453–487.

Edwards, J. M., and A. Slingo (1996), Studies with a flexible new radiation code. I: Choosing a configuration for a large-scale model, *Quart. J. Roy. Meteor. Soc.*, *122*(531), 689–719.

Fu, Q., and K. N. Liou (1993), Parameterization of the radiative properties of cirrus clouds, *J. Atmos. Sci.*, *50*(13), 2008–2025.

Geoffroy, O., J.-L. Brenguier, and I. Sandu (2008), Relationship between drizzle rate, liquid water path and droplet concentration at the scale of a stratocumulus cloud system, *Atmos. Chem. Phys.*, *8*(16), 4641–4654.

Heus, T., C. C. van Heerwaarden, H. J. J. Jonker, A. Pier Siebesma, S. Axelsen, K. van den Dries, O. Geoffroy, A. F. Moene, D. Pino, S. R. de Roode, and J. Vil-Guerau de Arellano (2010), Formulation of the dutch atmospheric large-eddy simulation (dales) and overview of its applications, *Geosci. Model Dev.*, *3*(2), 415–444.

Khairoutdinov, M., and Y. Kogan (2000), A new cloud physics parameterization in a large-eddy simulation model of marine stratocumulus, *Mon. Wea. Rev.*, *128*(1), 229–243.

Khairoutdinov, M. F., and D. A. Randall (2003), Cloud resolving modeling of the ARM summer 1997 IOP: Model formulation, results, uncertainties, and sensitivities, *J. Atmos. Sci.*, *60*(4), 607–625.

Krueger, S. K., G. T. McLean, and Q. Fu (1995), Numerical simulation of the stratus-to-cumulus transition in the subtropical marine boundary layer. part i: Boundary-layer structure, *J. Atmos. Sci.*, *52*(16), 2839–2850.

Martin, G. M., D. W. Johnson, D. P. Rogers, P. R. Jonas, P. Minnis, and D. A. Hegg (1995), Observations of the interaction between cumulus clouds and warm stratocumulus clouds in the marine boundary layer during ASTEX, *J. Atmos. Sci.*, *52*(16), 2902–2922.

Medeiros, B., and B. Stevens (2011), Revealing differences in gcm representations of low clouds, *Climate Dyn.*, *36*(1-2), 385–399.

Mlawer, E. J., S. J. Taubman, P. D. Brown, M. J. Iacono, and S. A. Clough (1997), Radiative transfer for inhomogeneous atmospheres: RRTM, a validated correlated-k model for the longwave, *J. Geophys. Res.*, *102*(D14), 16,663–16,682.

Morrison, H., J. A. Curry, and V. I. Khvorostyanov (2005), A new double-moment microphysics parameterization for application in cloud and climate models. part i: Description, *J. Atmos. Sci.*, *62*(6), 1665–1677.

Nicholls, S. (1984), The dynamics of stratocumulus: Aircraft observations and comparisons with a mixed layer model, *Quart. J. Roy. Meteor. Soc.*, *110*(466), 783–820.

Pawlowska, H., and J.-L. Brenguier (2000), Microphysical properties of stratocumulus clouds during ace-2, *Tellus B*, *52*(2), 868–887.

Pincus, R., and B. Stevens (2009), Monte carlo spectral integration: a consistent approximation for radiative transfer in large eddy simulations, *Journal of Advances in Modeling Earth Systems; Vol. 1, 2009*, pp. –.

Prusa, J. M., P. K. Smolarkiewicz, and A. A. Wyszogrodzki (2008), Eulag, a computational model for multiscale flows, *Computers & Fluids*, *37*(9), 1193–1207.

Renfrew, I. A., G. W. K. Moore, P. S. Guest, and K. Bumke (2002), A comparison of surface layer and surface turbulent flux observations over the Labrador sea with ECMWF analyses and NCEP reanalyses, *J. Phys. Oceanogr.*, *32*(2), 383–400.

Sandu, I., and B. Stevens (2011), On the factors modulating the stratocumulus to cumulus transitions, *J. Atmos. Sci.*, *68*(9), 1865–1881.

Sandu, I., B. Stevens, and R. Pincus (2010), On the transitions in marine boundary layer cloudiness, *Atmos. Chem. Phys.*, *10*(5), 2377–2391, doi:http://dx.doi.org/10.5194/acp-10-2377-2010.

Seifert, A., and K. D. Beheng (2001), A double-moment parameterization for simulating autoconversion, accretion and selfcollection, *Atmos. Res.*, *59-60*, 265–281.

Shutts, G. J., and M. E. B. Gray (1994), A numerical modelling study of the geostrophic adjustment process following deep convection, *Quart. J. Roy. Meteor. Soc.*, *120*(519), 1145–1178.

Sigg, R., and G. Svensson (2004), Three-dimensional simulation of the ASTEX Lagrangian 1 field experiment with a regional numerical weather prediction model, *Quart. J. Roy. Meteor. Soc.*, *130*(597), 707–724.

Smolarkiewicz, P. K. (2006), Multidimensional positive definite advection transport algorithm: an overview, *Int. J. Numer. Meth. Fluids*, *50*(10), 1123–1144.

Smolarkiewicz, P. K., and W. W. Grabowski (1990), The multidimensional positive definite advection transport algorithm: nonoscillatory option, *Journal of Computational Physics*, *86*(2), 355–375.

Stevens, B. (2002), Entrainment in stratocumulus-topped mixed layers, *Quart. J. Roy. Meteor. Soc.*, *128*(586), 2663–2690.

Stevens, B., and A. Seifert (2008), Understanding macrophysical outcomes of microphysical choices in simulations of shallow cumulus convection, *J. Meteor. Soc. Japan*, *86A*, 143–162.

Stevens, B., C.-H. Moeng, A. S. Ackerman, C. S. Bretherton, A. Chlond, S. de Roode, J. Edwards, J.-C. Golaz, H. Jiang, M. Khairoutdinov, M. P. Kirkpatrick, D. C. Lewellen,

A. Lock, F. Mller, D. E. Stevens, E. Whelan, and P. Zhu (2005), Evaluation of large-eddy simulations via observations of nocturnal marine stratocumulus, *Mon. Wea. Rev.*, *133*(6), 1443–1462.

Stevens, D. E., and S. Bretherton (1996), A forward-in-time advection scheme and adaptive multilevel flow solver for nearly incompressible atmospheric flow, *Journal of Computational Physics*, *129*(2), 284–295.

Svensson, G., M. Tjernström, and D. Koračin (2000), The sensitivity of a stratocumulus transition: Model simulations of the ASTEX first Lagrangian, *Bound.-Layer Meteor.*, *95*(1), 57–90.

Teixeira, J., S. Cardoso, M. Bonazzola, J. Cole, A. DelGenio, C. DeMott, C. Franklin, C. Hannay, C. Jakob, Y. Jiao, J. Karlsson, H. Kitagawa, M. Köhler, A. Kuwano-Yoshida, C. LeDrian, J. Li, A. Lock, M. J. Miller, P. Marquet, J. Martins, C. R. Mechoso, E. V. Meijgaard, I. Meinke, P. M. A. Miranda, D. Mironov, R. Neggers, H. L. Pan, D. A. Randall, P. J. Rasch, B. Rockel, W. B. Rossow, B. Ritter, A. P. Siebesma, P. M. M. Soares, F. J. Turk, P. A. Vaillancourt, A. Von Engeln, and M. Zhao (2011), Tropical and subtropical cloud transitions in weather and climate prediction models: The GCSS/WGNE pacific cross-section intercomparison (GPCI), *J. Climate*, *24*(20), 5223–5256.

Toon, O. B., C. P. McKay, T. P. Ackerman, and K. Santhanam (1989), Rapid calculation of radiative heating rates and photodissociation rates in inhomogeneous multiple scattering atmospheres, *J. Geophys. Res.*, *94*(D13), 16,287–16,301.

Van der Dussen, J. J., S. de Roode, and A. Siebesma (2012), Large eddy simulation sensitivity experiments of the ASTEX stratocumulus to cumulus transition, in *20th*

*Symposium on Boundary Layers and Turbulence.*

vanZanten, M. C., B. Stevens, G. Vali, and D. H. Lenschow (2005), Observations of drizzle in nocturnal marine stratocumulus, *J. Atmos. Sci.*, *62*(1), 88–106.

vanZanten, M. C., B. Stevens, L. Nuijens, A. P. Siebesma, A. S. Ackerman, F. Burnet, A. Cheng, F. Couvreux, H. Jiang, M. Khairoutdinov, Y. Kogan, D. C. Lewellen, D. Mechem, K. Nakamura, A. Noda, B. J. Shipway, J. Slawinska, S. Wang, and A. Wyszogrodzki (2011), Controls on precipitation and cloudiness in simulations of trade-wind cumulus as observed during RICO, *J. Adv. Model. Earth Syst.*, *3*(6), M06,001.

Vickers, D., and L. Mahrt (2010), Sea-surface roughness lengths in the midlatitude coastal zone, *Quart. J. Roy. Meteor. Soc.*, *136*(649), 1089–1093.

Wang, Q., and D. H. Lenschow (1995), An observational study of the role of penetrating cumulus in a marine stratocumulus-topped boundary layer, *J. Atmos. Sci.*, *52*(16), 2778–2787.

Wood, R. (2012), Stratocumulus clouds, *Mon. Wea. Rev.*, *140*, 2373–2423.

Wood, R., and C. S. Bretherton (2004), Boundary layer depth, entrainment, and decoupling in the cloud-capped subtropical and tropical marine boundary layer, *J. Climate*, *17*(18), 3576–3588.

Wyant, M. C., C. S. Bretherton, H. A. Rand, and D. E. Stevens (1997), Numerical simulations and a conceptual model of the stratocumulus to trade cumulus transition, *J. Atmos. Sci.*, *54*(1), 168–192.

Yamaguchi, T., and D. A. Randall (2012), Cooling of entrained parcels in a large-eddy simulation, *J. Atmos. Sci.*, *69*(3), 1118–1136.

Yamaguchi, T., D. A. Randall, and M. F. Khairoutdinov (2011), Cloud modeling tests of the ULTIMATE-MACHO scalar advection scheme, *Mon. Wea. Rev.*, *139*(10), 3248–3264.

Zhang, M., C. Bretherton, M. Webb, and A. Siebesma (2010), CFMIP-GCSS intercomparison of large eddy models and single column models (CGILS), *GEWEX News*, *20*, 6–8.

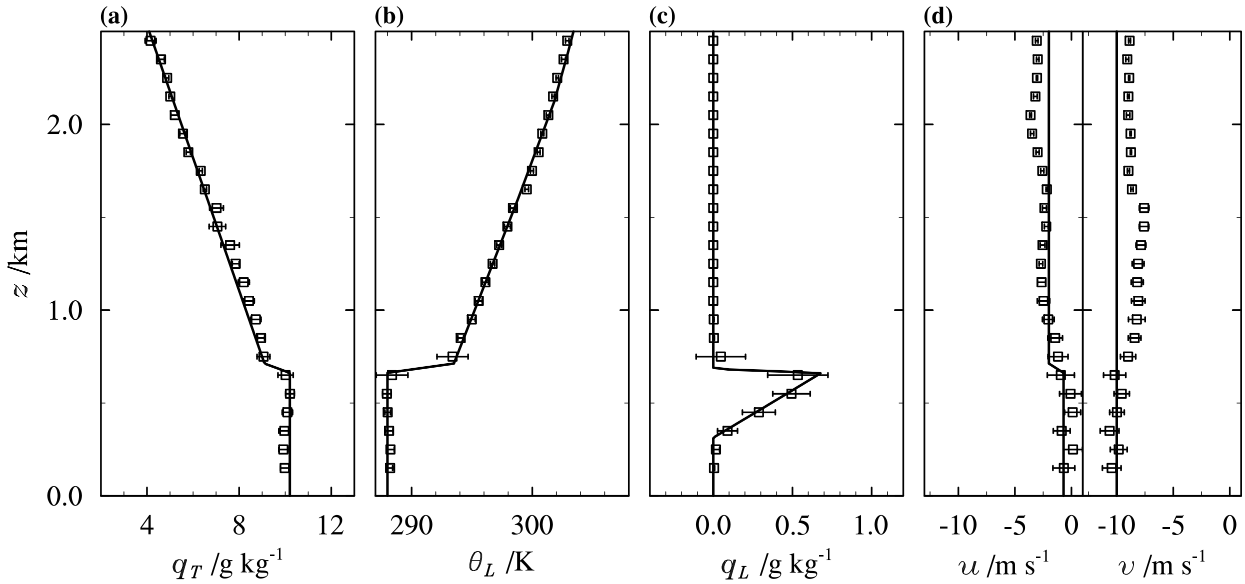


**Figure 1.** Initial profiles of total humidity $q_T$ (a), liquid water potential temperature $\theta_L$ (b), liquid water specific humidity $q_L$ (c) and horizontal velocities $u$ (east-west) and $v$ (south-north) (d). Squares denote observations, gathered during the second research flight (A209) of the First Lagrangian, bin-averaged over height intervals of 100 m. Error bars show the ± one standard deviation range.

**Table 1.** Values of the parameters, used with Eq. (1) to describe the initial profiles of the relevant variables.

| $\varphi$ | $\varphi_{ml}$ | $\Delta\varphi$ | $\Gamma_\varphi$ (km$^{-1}$) |
|---|---|---|---|
| $q_T$ (g kg$^{-1}$) | 10.2 | $-1.1$ | $-2.8$ |
| $\theta_L$ (K) | 288.0 | 5.5 | 6.0 |
| $u$ (m s$^{-1}$) | $-0.7$ | $-1.3$ | 0.0 |
| $v$ (m s$^{-1}$) | $-10.0$ | 0.0 | 0.0 |

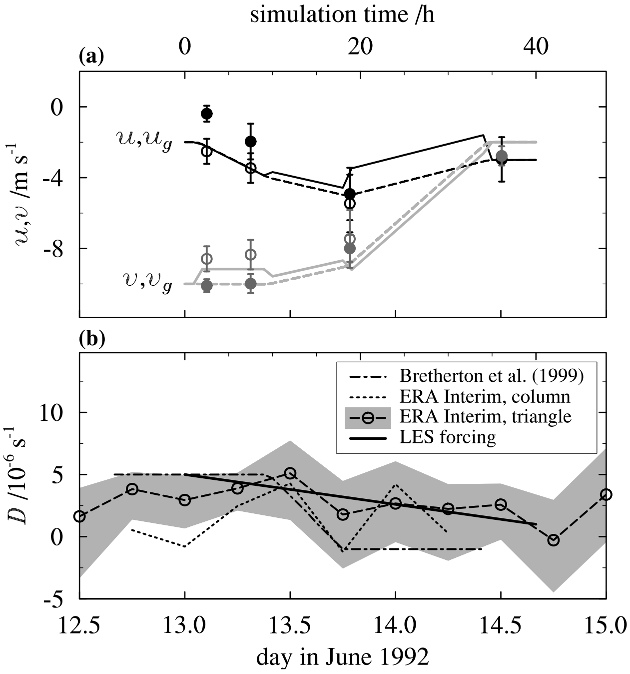


**Figure 2.** Plot of the geostrophic wind (solid lines) and the expected horizontal velocities calculated using Eqs. (2) (dashed) as a function of time, as well as the observed boundary layer (closed circles) and free atmospheric velocities (open circles) (a). Figure (b) shows the boundary layer averaged divergence of the horizontal winds, derived from ERA-40 data by *Bretherton et al.* [1999] (dash-dotted). The dotted line was obtained by taking a weighted area and a boundary layer average of the divergence from ERA-Interim data, along the trajectory as reported by *Bretherton and Pincus* [1995]. The dashed line is the divergence in the boundary layer, averaged over the ASTEX triangle [*Albrecht et al.*, 1995]; the area between the 20th and the 80th percentile has been shaded in grey. The divergence selected for the simulations is indicated by the solid black line.

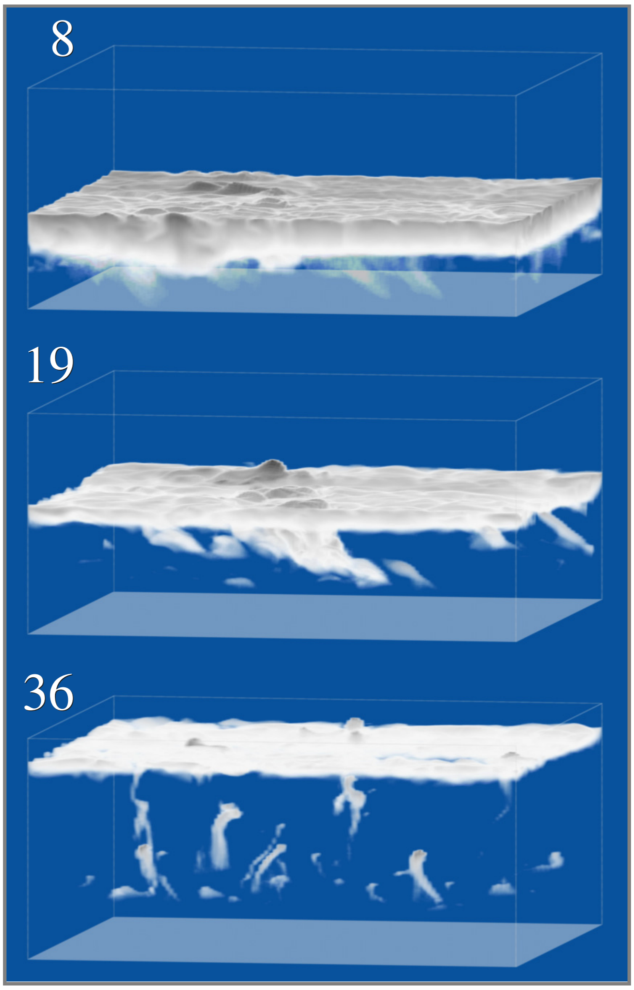


**Figure 3.** Snapshots of the cloud liquid water including rain water, from top to bottom, hours 8, 19 and 36 as simulated using DALES. High $q_L$ values have a darker shade and are more oblique. The white plane indicates the surface. The total height of the shown domain is 2 km.

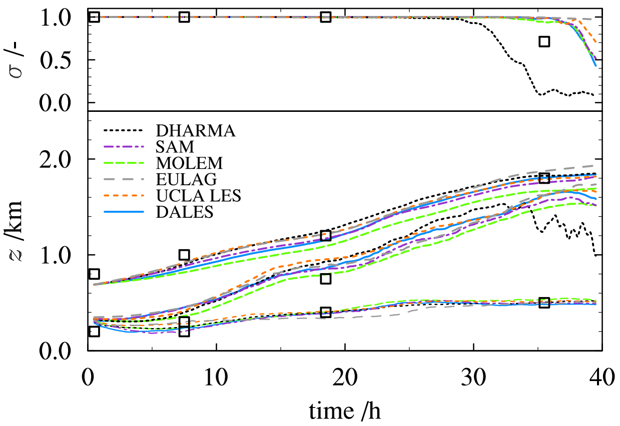


**Figure 4.** The total cloud cover (top) and the contours of the simulated clouds (bottom) composed of the inversion height $z_i$ (as an indication of the mean stratocumulus cloud top), minimum cloud base height $z_{b,\mathrm{min}}$ and mean cloud base height $z_b$, for each of the models shown in the legend. The squares denote similar quantities, estimated from the profiles of $q_L$ shown in the next section.

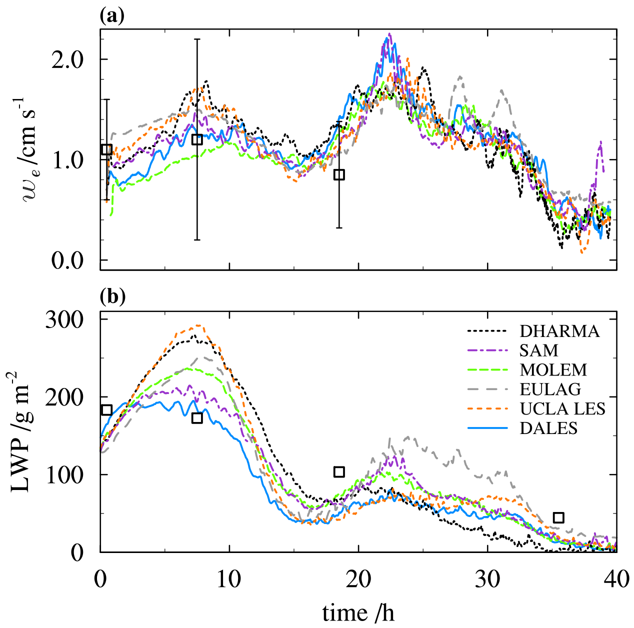


**Figure 5.** The entrainment rate $w_e$ (a) and the liquid water path LWP (b) as a function of time for the models indicated in the legend. Estimates based on observations of $w_e$, including uncertainties were obtained from *De Roode and Duynkerke* [1997], while the values of the LWP where obtained by integrating the mean $q_L$ profiles, shown in Figure 7. A running averaging filter with a width of 1 h has been applied on the entrainment rates from the simulations.

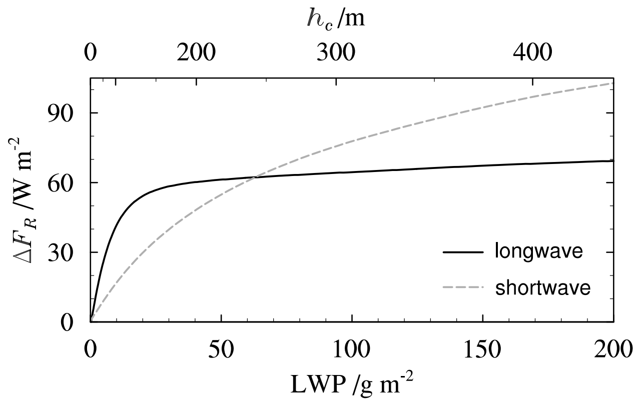


**Figure 6.** The difference in total longwave as well as shortwave radiative flux between the top and the base of an adiabatic stratocumulus cloud layer as a function of LWP (bottom axis) and of cloud thickness $h_c$ (top axis). The Fu-Liou based radiative transfer code that is used in DALES and UCLA LES was used to perform the calculations. By varying the total humidity in the mixed layer $q_{T,\mathrm{ml}}$ in Eq. (1), different values for the liquid water path were obtained. The solar radiation fluxes are calculated at local noon, 13 UTC, and a cloud droplet number density of $N_c = 100\,\mathrm{cm}^{-3}$ was used.

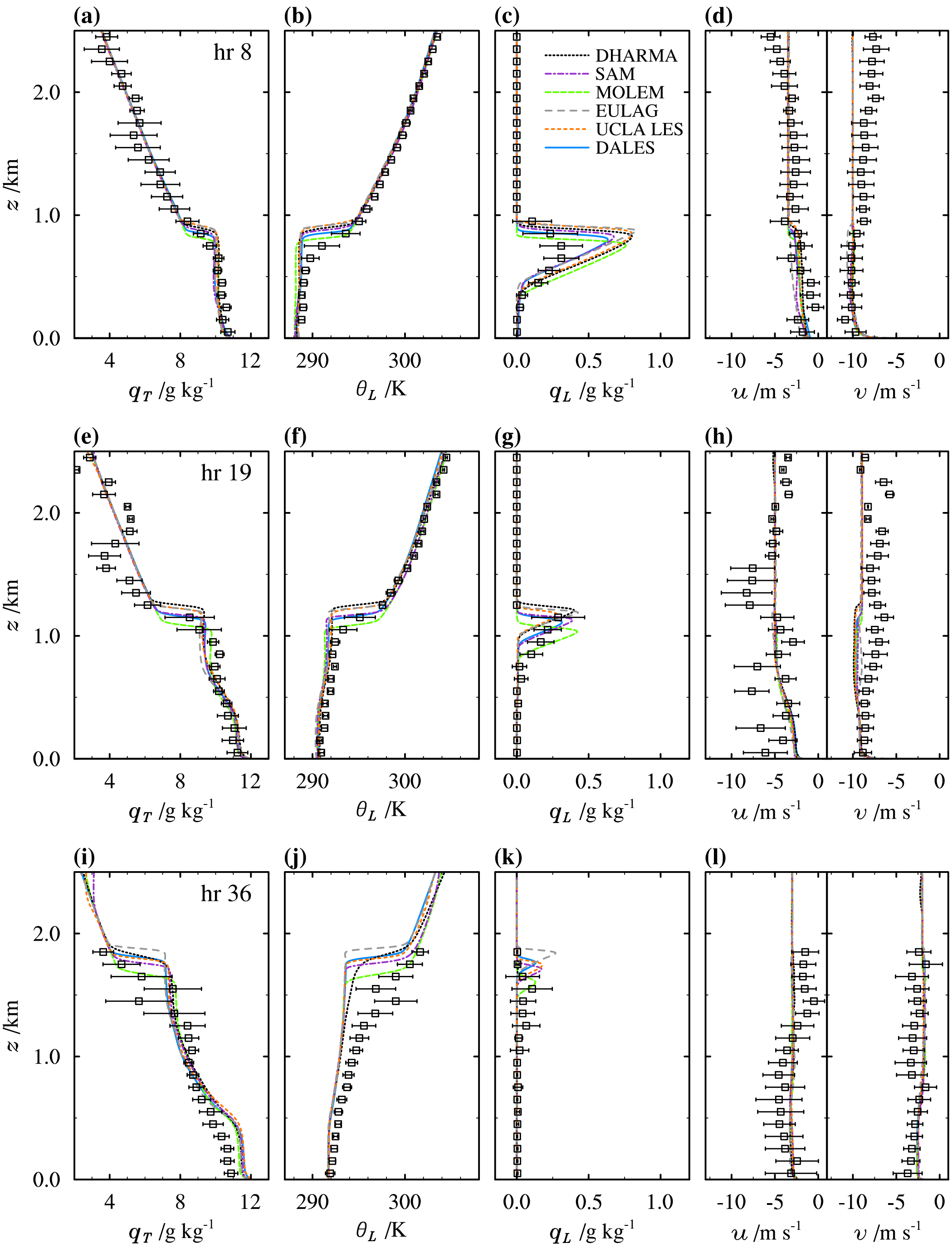


**Figure 7.** The domain averaged simulation results of the mean state variables $q_T$, $\theta_L$, $q_L$ and the horizontal velocities $u$ and $v$ as a function of height for ASTEX flights RF06 (a)-(d), RF07 (e)-(h) and A210 (i)-(l). Lines styles and colors according to the legend. The black squares denote bin-averaged observations with the $\pm\sigma$ range indicated by the error bars.

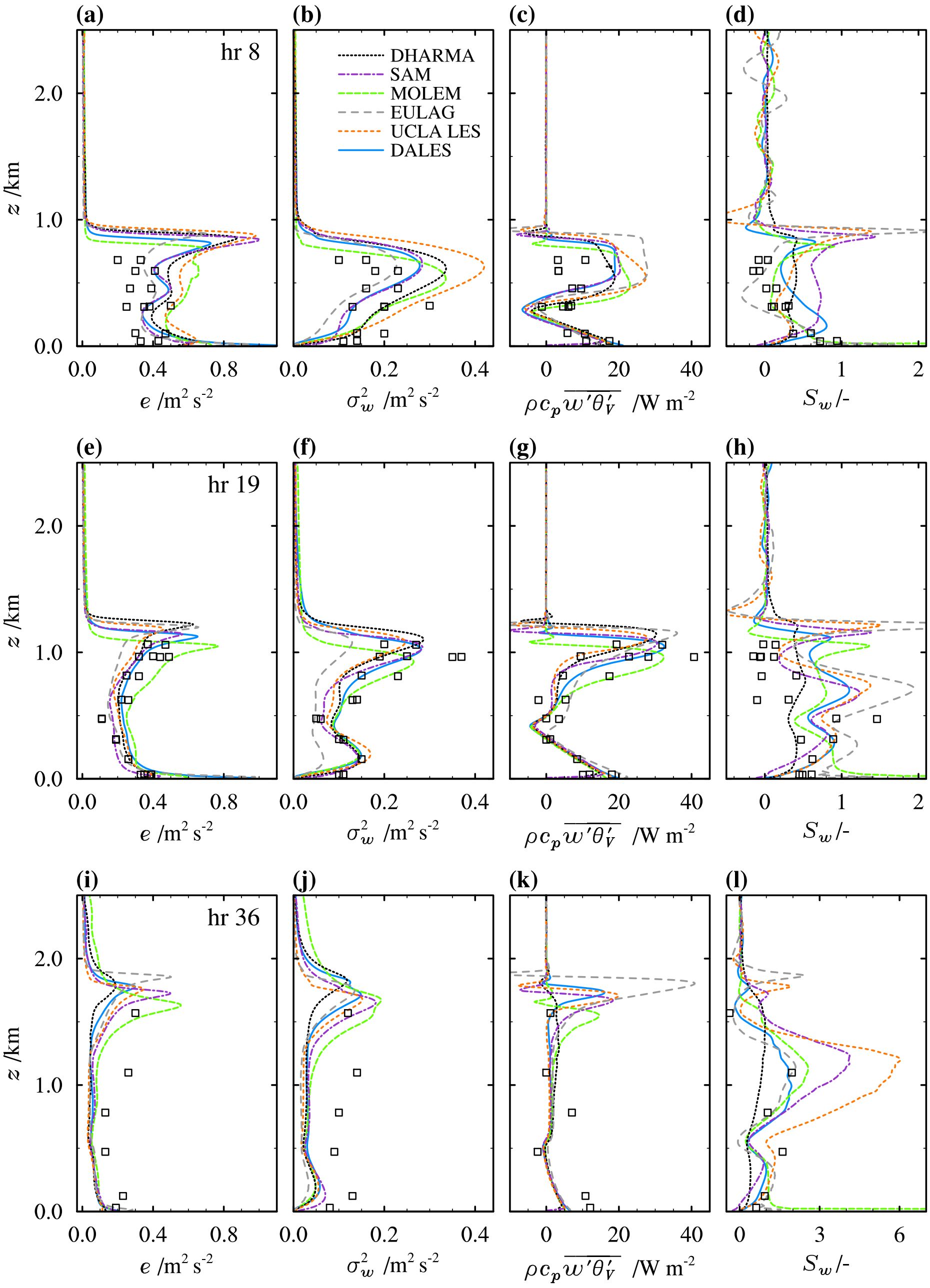


**Figure 8.** Vertical profiles of domain averaged turbulence statistics: the turbulent kinetic energy $e$, the vertical velocity variance $\sigma_w^2$, the virtual potential temperature flux $\overline{w'\theta_V'}$ and the vertical velocity skewness $S_w$, for ASTEX flights RF06 (a)-(d), RF07 (e)-(h) and A210 (i)-(l). Lines styles and colors are according to the legend. The black squares denote observations derived from measurement time series, performed during horizontal flight legs. Note the different scale of the horizontal axis in Figure 8l.

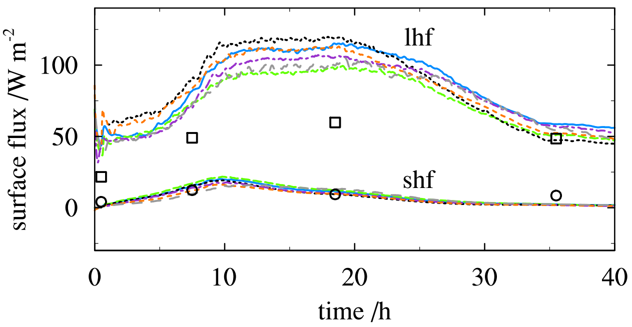


**Figure 9.** The surface fluxes of latent (upper set of lines and squares) and sensible heat (lower set and circles) as a function of time for the models indicated in the legend in Figure 7. The squares and circles denote observations obtained from the flight legs flown closest to the surface at approximately 30 m height.

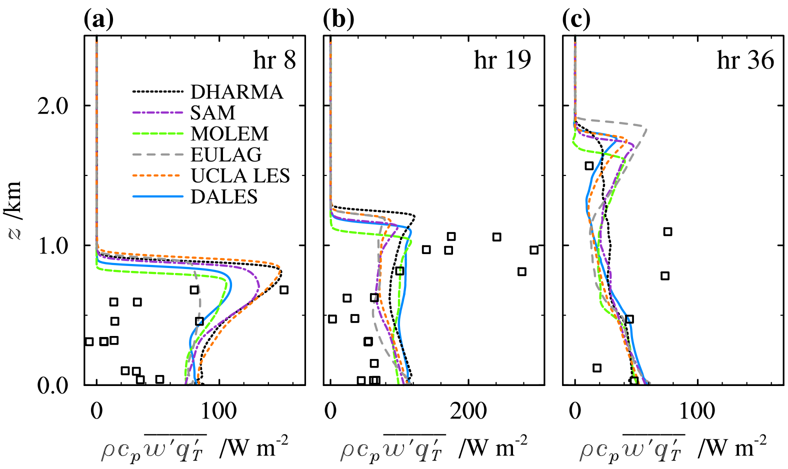


**Figure 10.** Domain averaged profiles of the turbulent fluxes of $q_T$ for the hours corresponding to flights RF06 (a), RF07 (b) and A210 (c). The black squares denote observations. Note the different scale of the horizontal axis in Figure (b).

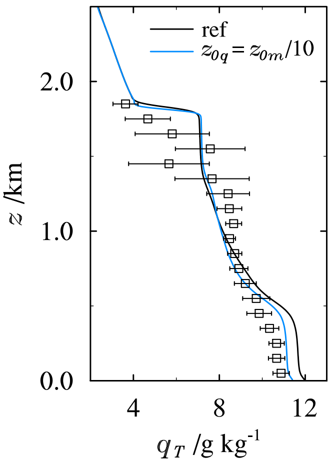


**Figure 11.** Horizontally averaged $q_T$ profiles for the reference simulation (black) as well as the simulation with $(z_{0q}, z_{0h}) = z_{0m}/10 = 0.02\,\text{mm}$ (blue) at hour 36 of the simulation.

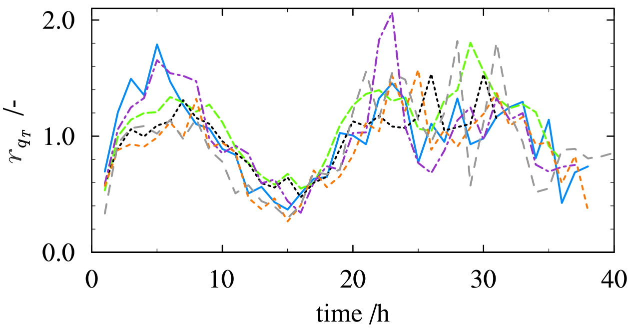


**Figure 12.** The ratio $r_{q_T}$ of the humidity flux at mean cloud base $z_b$ to the surface flux defined in Eq. (14). Legend as in Figure 7. The series are cut off as soon as the average cloud cover drops below 0.95.

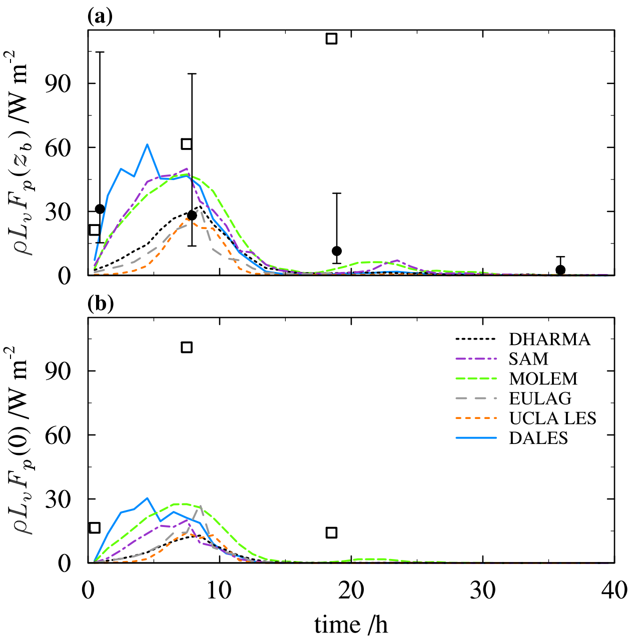


**Figure 13.** The precipitation rate $F_p$ in units of $\mathrm{W\,m^{-2}}$ at mean cloud base height $z_b$ (a) and at the surface (b) for the models denoted in the legend. Squares denote average precipitation rates obtained from the flight legs that were flown closest to the mentioned levels. The black dots show parametrised precipitation rates at $z_b$ calculated using Eq. (15) with a cloud droplet number concentration $N_c = 100\,\mathrm{cm^{-3}}$, while the error bars indicate the range of precipitation rates spanned using $N_c = 50$ and $150\,\mathrm{cm^{-3}}$.

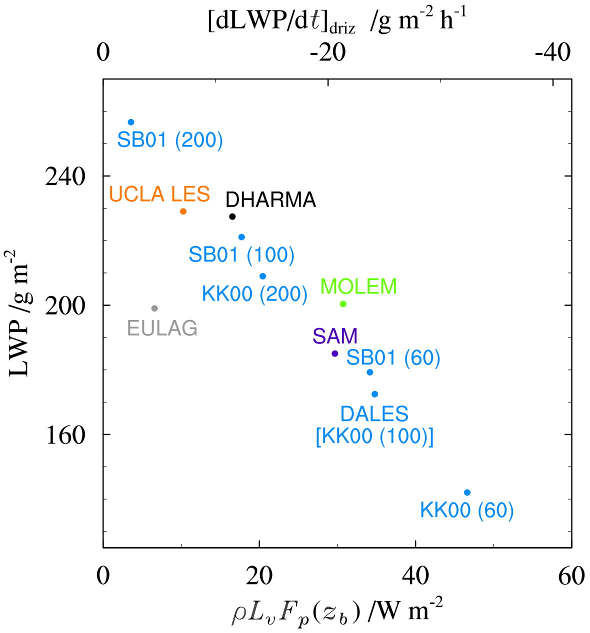


**Figure 14.** Scatter plot of the time averaged LWP as a function of time averaged precipitation rate at stratocumulus cloud base. Both were averaged over the first 12 hours of the transition. The top axis shows the precipitation rate in terms of a LWP tendency in $\mathrm{g\,m^{-2}\,h^{-1}}$. The labels indicate the model or the microphysics scheme (in DALES) used, while the numbers between the parentheses indicate the cloud droplet number density in $\mathrm{cm^{-3}}$.

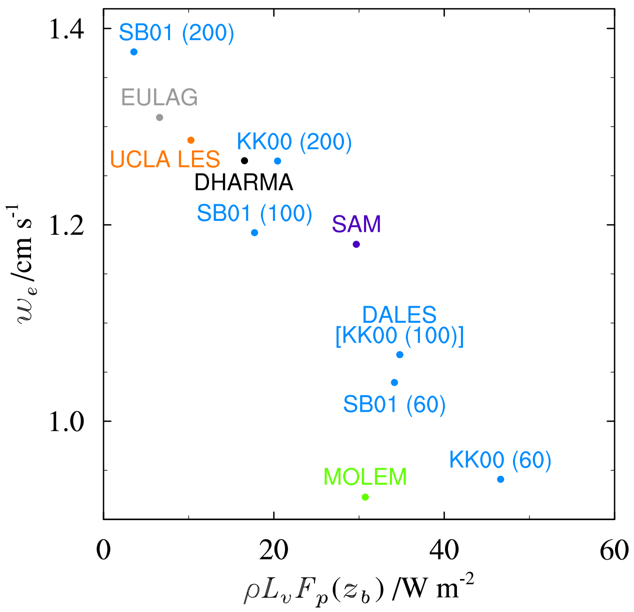


**Figure 15.** As Figure 14, but here for the entrainment rate $w_e$, averaged over the first 12 hours of the transition.

**Table 2.** List of the participating modellers and the used models, including parametrisation schemes.

| Modeller | Model | Model description | Microphysics | Radiation | Advection |
|---|---|---|---|---|---|
| A. Ackerman | DHARMA | *Stevens* [2002] | *Morrison et al.* [2005] | *Toon et al.* [1989] | *Stevens and Bretherton* [1996] |
| P. Blossey | SAM 6.8.2 | *Khairoutdinov and Randall* [2003] | *Khairoutdinov and Kogan* [2000] | *Mlawer et al.* [1997, RRTMG] | *Smolarkiewicz and Grabowski* [1990] |
| M. Kurowski | EULAG | *Prusa et al.* [2008] | *Khairoutdinov and Kogan* [2000, single moment] | *Briegleb* [1992] | *Smolarkiewicz* [2006] |
| A. Lock | MOLEM | *Shutts and Gray* [1994]; *Abel and Shipway* [2007] | *Abel and Shipway* [2007] | *Edwards and Slingo* [1996] | *Yamaguchi et al.* [2011] |
| I. Sandu | UCLA LES | *Stevens and Seifert* [2008] | *Seifert and Beheng* [2001] | *Fu and Liou* [1993]; *Pincus and Stevens* [2009] | *Stevens et al.* [2005] |
| J. van der Dussen | DALES 3.2 | *Heus et al.* [2010] | *Khairoutdinov and Kogan* [2000] | *Fu and Liou* [1993]; *Pincus and Stevens* [2009] | *Blossey and Durran* [2008] |

**Table 3.** Summary of the flight details [for more information, see *De Roode and Duynkerke*, 1997, Table 1].

| Flight | UTC time (date) | Simulation time |
|---|---|---|
| RF05 | 1719-2133 (12 June) | - |
| A209 | 0032-0426 (13 June) | Initialisation |
| RF06 | 0451-1013 (13 June) | 8th hour average |
| RF07 | 1627-2109 (13 June) | 19th hour average |
| A210 | 1111-1302 (14 June) | 36th hour average |